

Article

Growth and Dielectric Properties of Ta-Doped $\text{La}_2\text{Ti}_2\text{O}_7$ Single Crystals

Hui Wang ^{1,2}, Qin Li ², Chaoyue Wang ², Huan He ², Jianding Yu ^{2,*} and Jiayue Xu ^{1,*}

¹ School of Materials Science and Engineering, Shanghai Institute of Technology, Shanghai 201418, China; zhifeiji0613@163.com

² Shanghai Institute of Ceramics, Chinese Academy of Science, Shanghai 200050, China; liqin@mail.sic.ac.cn (Q.L.); cywang@mail.sic.ac.cn (C.W.); ch.hh@mail.sic.ac.cn (H.H.)

* Correspondence: yujianding@mail.sic.ac.cn (J.Y.); xujiayue@sit.edu.cn (J.X.); Tel.: +86-021-5241-2503 (J.Y.); +86-021-6087-3581 (J.X.)

Received: 20 November 2017; Accepted: 13 February 2018; Published: 27 February 2018

Abstract: High-quality Ta-doped $\text{La}_2\text{Ti}_2\text{O}_7$ (Ta-LTO) single crystal of about 40 mm in length and 5 mm in diameter was successfully prepared by the optical floating zone method. An X-ray rocking curve reveals that the crystal of LTO has excellent crystalline quality. As-grown crystals were transparent after annealing in air and the transmittance is up to 76% in the visible and near-infrared region. X-ray diffraction showed that this compound possessed a monoclinic structure with $P2_1$ space group. The dielectric properties were investigated as functions of temperature (0–300 °C) and frequency (10^2 Hz– 10^5 Hz). Dielectric spectra indicated an increase in the room-temperature dielectric constant accompanied by a drop in the loss tangent as a result of the Ta doping. One relaxation was observed in the spectra of electric modulus, which was ascribed to be related to the oxygen vacancy. The dielectric relaxation with activation energy of 1.16 eV is found to be the polaron hopping caused by the oxygen vacancies.

Keywords: Ta-LTO single crystal; floating zone method; dielectric properties; oxygen vacancy

1. Introduction

With the recent progress and development in chemical and material processing, automotive, aerospace, and power-generating industries, there has been an ever-increasing need for actuators and sensors that can be operated at high temperatures [1–3]. For example, nuclear reactors need to be monitored during operation, and the temperature can be reached above 1000 °C [1,2]. Similarly, aerospace engines have working temperature at above 900 °C [1,2]. They both require a high-temperature sensor to monitor the operation situation. In the past several decades, most studies on high-temperature piezoelectric or ferroelectric have focused on a range of single crystals based on gallium phosphate (GaPO_3), lithium niobate (LiNbO_3 , LN), langasites with general formula, $\text{Ca}_3\text{TaAl}_3\text{Si}_2\text{O}_{14}$, and oxyborate [$\text{ReCa}_4\text{O}(\text{BO}_3)$] (Re is rare earth element) [1,2,4–7]. Low Curie point, high cost and poor mechanical properties have limited their practical applications at very high temperature. So it is of great significance to develop piezoelectric materials with high T_c to meet urgent requirements for high-temperature applications.

Ferroelectric materials with a perovskite-like layered structure (PLS) have caught attention due to the highest Curie temperature [8,9]. Generally, the PLS structure with a formula of $\text{A}_n\text{B}_n\text{O}_{3n+2}$ is characterized by corner-shared BO_6 octahedron and 12-coordinated A cations within the perovskite-like layered separated by oxygen-rich gaps [10,11]. Among all these PLS ferroelectrics, $\text{La}_2\text{Ti}_2\text{O}_7$ (LTO) is a promising candidate for actuators and sensors at extremely high temperature ($T_c = 1500$ °C). Masakazu et.al had reported the LTO single crystal for the first time in 1972 [12]. The piezoelectric coefficient (d_{22}) and relative permittivity (ϵ) of LTO single crystal had been reported to be 16 pC/N

and 42–62, respectively [9]. The ferroelectric and piezoelectric properties of LTO had been studied in the form of polycrystalline ceramics and thin films [13–20]. In addition, Ni-doped LTO has been found to have good photocatalytic activity in the water-splitting reaction [21] and in the oxidative decomposition of CH_3Cl [22]. Cai et al. [23] found that Graphitic- C_3N_4 hybridized N-doped LTO two-dimensional layered composites as an efficient visible-light-driven photocatalyst. Also, a series of ceramics with a general formula $\text{La}_2\text{Ti}_{2-x}\text{Ta}_x\text{O}_7$ ($x = 0.05, 0.1, 0.2$ and 0.3) were prepared by Spark Plasma Sintering [24].

However, LTO and Ta-doped LTO single crystals have barely been reported. On the one hand, their melting points are very high and volatile; on the other hand, they are easily cleaved due to the special layered structure. Generally speaking, it was difficult to prepare a single crystal, since the piezoelectric properties are closely related to the dielectric properties, and in lead zirconate titanate (PZT), pentavalent donor additions (tantalum) were reported to produce significant effects on the mechanical and electrical properties characterized by enhanced dielectric constant and DC resistivity [25]. Therefore this motivated us to study effects of tantalum substitution on the structure and dielectric properties of $\text{La}_2\text{Ti}_2\text{O}_7$. A thorough understanding of the dielectric properties is of vital importance.

In the present work, we successfully prepared the LTO and Ta-doped LTO single crystals using optical floating zone method (OFZ). The scanning electron microscope (SEM) with energy-dispersive X-ray (EDX) experiment used a field emission scanning electron microscope Hitachi SU8220 manufactured by Hitachi, Japan. The XRD patterns were recorded in the range 10° – 70° , with a step of 0.02° and with a speed of $2^\circ/\text{min}$, using a Rigaku Ultima IV X-ray diffractometer equipped with Cu anticathode ($\lambda\alpha_1 = 1.54059$ nm), nickel foil filter used to attenuate Cu $k\beta$ radiation and Soller slits to limit the divergence of X-ray beam. The transmittance (Varian Cary-5000, Agilent, Varian, Palo Alto, CA, USA) of LTO and Ta-LTO single crystals in visible and near-infrared region were measured. Besides, detailed investigations on the frequency (10^2 Hz– 10^5 Hz) dielectric properties of Ta-doped LTO single crystal over a wide temperature range from 0 – 300 °C were performed. The dielectric properties were measured on a precise impedance analyzer dielectric measuring system (Broadband Dielectric/Impedance Spectrometer, Novocontrol Technologies GmbH and Co. KG, Germany).

2. Experimental Details

High-purity powders of La_2O_3 (purity 99.99%, Sinopharm Chemical Regent, Shanghai, China), TiO_2 (Purity 99.99%, imported from Japan) and Ta_2O_5 (Purity 99.99%, Aladdin, Shanghai, China) were mixed in a stoichiometry of $\text{La}_2\text{Ti}_2\text{O}_7$ and $\text{La}_2\text{Ti}_{1.98}\text{Ta}_{0.02}\text{O}_7$ chemical formula. They were milled in the presence of absolute ethanol for 24 h. After being dried and screened, the mixture was calcined at 1300 °C for 8 h in air with an intermediate grinding to improve its homogeneity. Then, the well-mixed powders were ground and formed into round rods using a cold isostatic pressure of 200 MPa. The rods were then sintered at 1200 °C– 1500 °C for 5–8 h in air. The typical dimensions of the sintered rod were 7–9 mm in diameter and 60–80 mm in length. The polycrystalline rods were used as feed and seed rods.

The crystal growth experiments were carried out by the OFZ technique with four ellipsoidal mirrors (FZ-T4000H), using four 4.0 KW halogen lamps as heat sources and the LabVIEW control system. The feed rod was suspended at the upper shaft and the seed was attached to the lower shaft. Both the feed rod and seed rod moved downwards and the melting zone was formed. The feed and seed shafts rotated at 15 rpm in the opposite direction and the crystal was grown from the bottom to top in a vertical direction, and the growth rate was 4–6 mm/h.

In this work, we have grown single crystals in an argon atmosphere and crack-free single crystals were obtained. The as-grown single crystals were annealed in air at 1200 °C for 1 h to eliminate thermal stress and reduce oxygen vacancy, then were naturally cooled down to room temperature. We have randomly selected two pieces of crystal from the big Ta-LTO crystals. One of them was characterized by energy-dispersive X-ray (EDX). The other was ground into powder to measure the

X-ray diffraction. In order to check the crystal perfection, a (100) wafer of LTO crystal was carefully polished for measuring the rocking curve by high resolution X-ray diffraction (HR-XRD). The crystals were cut into several slices perpendicular to the direction of growth and then polished. The prior growth direction was (622) determined by X-ray orientation.

3. Result and Discussion

The melting point of tantalum oxide is higher than lanthanum oxide, so it is more difficult to grow Ta-doped LTO solution crystals at higher temperature. Considering the melting point (1790 °C) and furnace power (1.94 KW) of LTO crystals, we adopted furnace power of 2.16 KW to grow Ta-LTO crystals in an argon atmosphere. By optimizing growth parameters, we have successfully grown the LTO and Ta-LTO single crystals, and a typical as-grown Ta-LTO single crystal boule is shown in Figure 1a. The Ta-LTO single crystal without annealing is black and non-transparent because of oxygen vacancy. The Figure 1b is the Ta-LTO single crystal after annealing for 1 h at 1200 °C in air. Annealing not only eliminated the thermal stress, but also reduced the oxygen vacancy and made the single crystal transparent. Oh et al. had suggest that the post-annealing effect, which involves a reduction in carrier concentration, originates with the loss of oxygen vacancies in the contact region by absorbing the oxygen present in the annealing atmosphere [26]. One sample was cut directly from the Ta-LTO single crystal boule perpendicular to the growth direction, then polished as shown in Figure 1c. Some cracks can be seen in Figure 1b. After the X-ray diffraction orientation, it is found that these cracks are due to incomplete cleavage along (400) direction consistent with pure LTO as Figure 1d [9]. Figure 2 shows the X-ray rocking curve of the LTO crystal. The profile of the (400) Bragg-reflections has a symmetrical peak with a full width at half maximum (FWHM) of 19.4 arcsec. The nearly perfect shape without any shoulder clarified the absence of any sub-grain, indicating the excellent quality of the LTO crystals.

The schematic diagram of the growth direction specimen of Ta-LTO single crystal wafer and the XRD of the Ta-LTO crystal wafer after annealing are shown in Figure 3, respectively. The Ta-LTO single crystals were grown by spontaneous nucleation. The prior growth direction was (622) determined by X-ray orientation. The energy-dispersive X-ray (EDX) images of Ta-LTO single crystal were shown in Figure 4. The results showed the composition homogeneity.

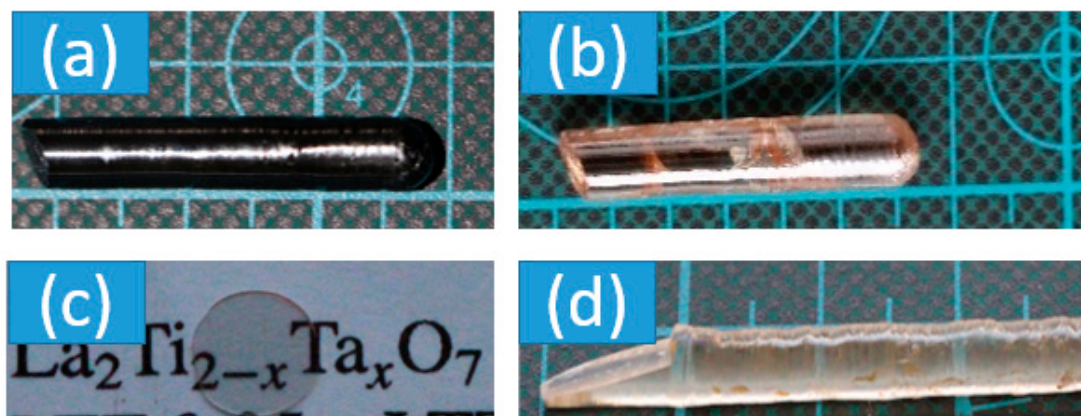


Figure 1. Ta-LTO single crystal grown by spontaneous nucleation with optical floating zone method (a) Ta-LTO single crystal was annealed for 1 h at 1200 °C; (b) Ta-LTO crystal wafer after annealing; (c) LTO single crystal by floating zone method (d).

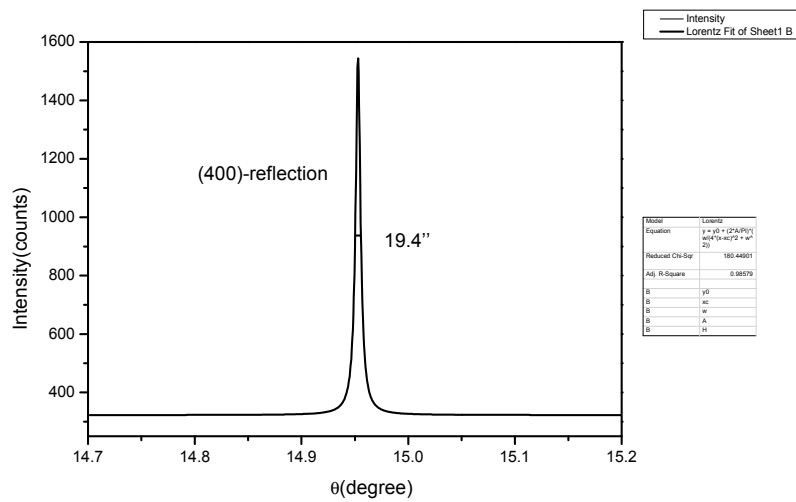


Figure 2. X-ray rocking curve of LTO single crystal.

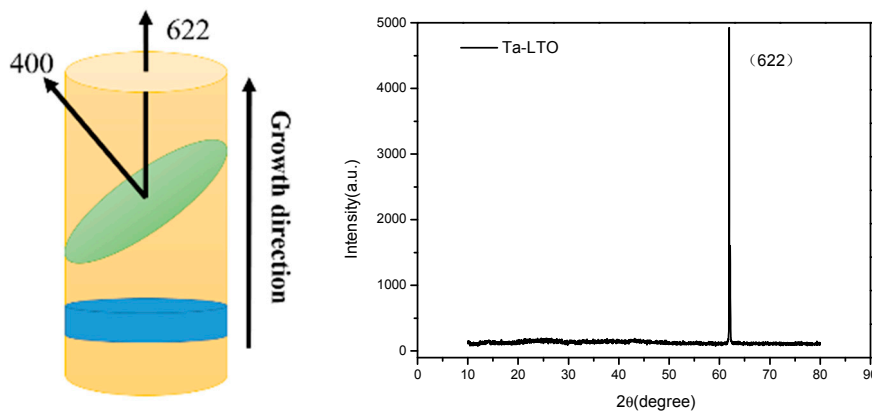


Figure 3. The schematic diagram of the growth direction specimen of Ta-LTO single crystal (Left) and the XRD of the Ta-LTO crystal wafer (Right).

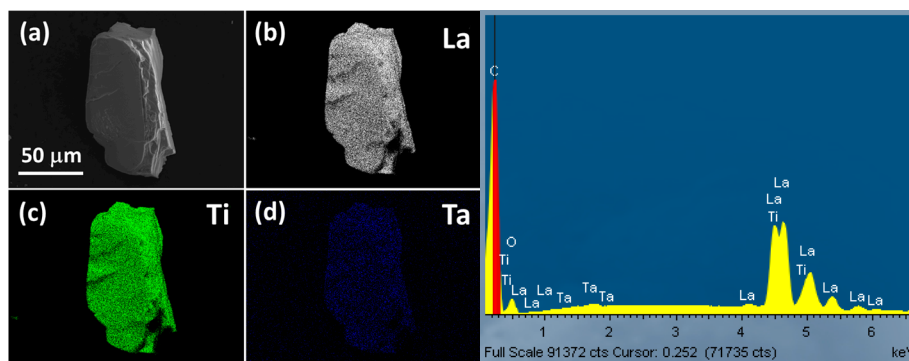


Figure 4. EDX images of Ta-LTO single crystal. (a): Ta-LTO (b): La (c):Ti (d):Ta.

The XRD patterns of the LTO and Ta-LTO powder samples at room temperature were shown in Figure 5. It can be noted that the main phase of Ta doped LTO was the same as LTO. All the peaks were successfully indexed based on a monoclinic crystal structure with $P2_1$ space group. As is shown in the inset, we can see that the position of the corresponding peak move to a large diffraction angle compared with LTO. The lattice parameters calculated with Jade 6.0 software are $a = 12.94924(3) \text{ \AA}$, $b = 5.56649(4) \text{ \AA}$, and $c = 7.81266(3) \text{ \AA}$. Compared to LTO [9], it is observed that both b and c increased

slightly with Ta doping, whereas a exhibited an obvious decrease. Generally, Ta ions replace Ti ions and the Ta ion (0.65 \AA) radius are larger than Ti (0.604 \AA) [27], which induce an expansion of the crystal structure. Similar phenomena can be seen in indium-doped barium hexaferrites [28].

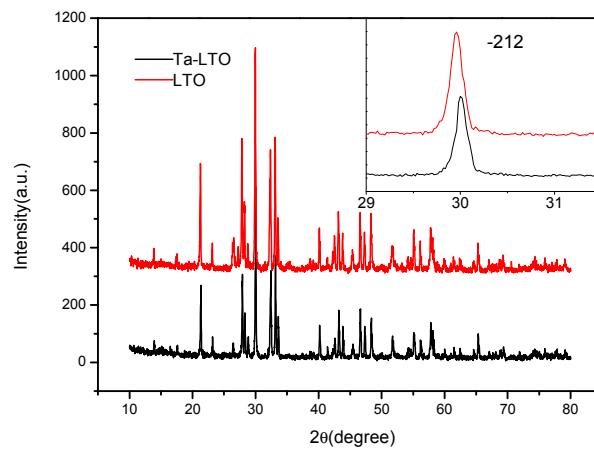


Figure 5. XRD patterns of the Ta-LTO and $\text{La}_2\text{Ti}_2\text{O}_7$ crystalline powder. The inset shows the magnified patterns of main peak.

Figure 6 shows the transmission spectrum of Ta-LTO and LTO crystals. It is transparent in the wavelength range of 350–900 nm and both of the transmittance are about 70%. Compared to the transmittance spectrum of Ta-LTO and LTO single crystals, we can see that the absorption edge shifted to infrared direction due to doping Ta_2O_5 into LTO single crystals.

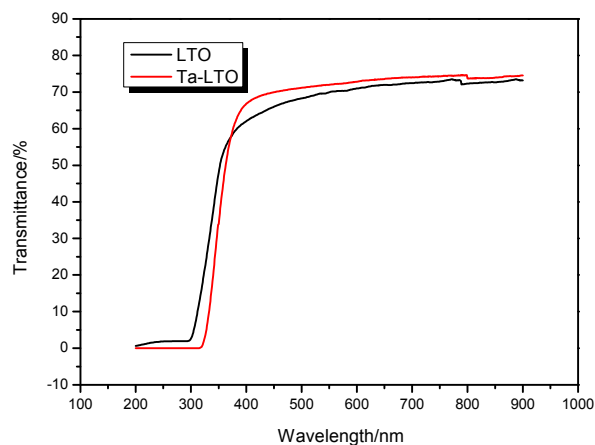


Figure 6. Transmission spectrum of Ta-LTO and LTO single crystals (0.02 mm).

The temperature dependences of the dielectric constant and dielectric loss tangent at various frequencies of LTO and Ta-LTO single crystals are shown in Figure 7a,b, respectively. From Figure 7a, we can see that dielectric constant for LTO crystals are almost independent of frequency and temperature in the low-temperature range from 0–100 °C. However, when the temperature is over 100 °C, the loss tangent in the form of index increased. This may be attributed to the larger conductivity due to oxygen vacancies. Although the Ta-LTO crystal changed from black to transparent after annealing at 1200 °C, it still has some oxygen vacancies. As the temperature increases, the movement speed of the oxygen vacancy increases rapidly, leading to the increase in current. In Figure 7b, it can be seen that the dielectric constant for Ta-LTO crystals are almost independent of frequency and temperature in the low-temperature range from 0–150 °C. This behavior indicates that Ta-LTO shows an intrinsic dielectric response resulting from the electronic and/or ionic polarization in the

low-temperature range [29,30]. The dielectric constant plateau of Ta-LTO shows a value of ~ 68 as Figure 7b, which is higher than the dielectric constant of LTO as shown in Figure 7a, so Ta doping can improve the dielectric properties of LTO. As shown in the inset of Figure 7a,b, the dielectric loss tangent of Ta-LTO crystal was lower than LTO crystal, which is more suitable for practical applications. It is worth noting that the frequency-dependent dielectric permittivity of Ta-LTO remarkably increases as the temperature increases above 200 °C, and $\tan\delta(T)$ increases rapidly with increasing temperature, causing pronounced background. The remarkable background in high temperature is usually caused by conductivity [31]. In this case, we applied the electric modulus, which is a powerful function for revealing background-obscured relaxation [30]. We, therefore, resort to the electric modulus.

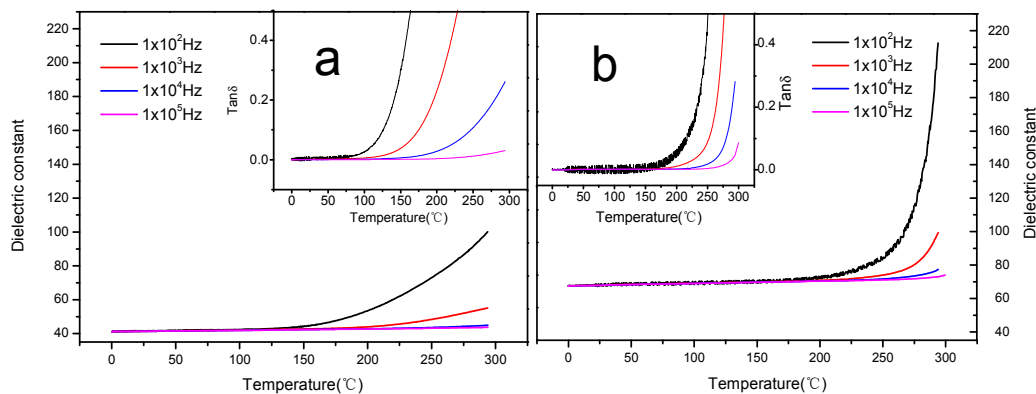


Figure 7. Temperature dependence of dielectric constant and $\tan\delta$ at various frequencies from 10^2 Hz to 10^5 Hz. (a) for LTO single crystal and (b) for Ta-LTO single crystal.

Figure 8a shows the imaginary part of the electric modulus M'' as a function of frequency in the temperature range from 398 K to 573 K. We can clearly see that M'' registers a peak whose position shifts to a higher temperature with increasing frequency. Meanwhile, the relaxation cannot be observed in the spectra of dielectric constants, indicating that electric modulus is a “good” dielectric function in revealing dielectric relaxation in the absence of a well-defined peak in $\tan\delta(T)$ or dielectric constant. It is well known that there are two sources contributing to the dielectric permittivity in the high-temperature range: the dielectric relaxation and the conductivity. When the conductivity contribution surpasses the relaxation contribution, especially in the high-temperature range, the relaxation is merged by the background. Since the electric modulus is defined as $M^* = M' + jM'' = 1/\epsilon^*$, the higher values of the background and the smaller values of M'' can be obtained. Therefore, the electric modulus can greatly lessen the background and become a “good” dielectric function in revealing the background-merged relaxation. The relaxation parameter can be obtained in terms of Arrhenius law

$$f = f_0 \exp(E_a/k_B T_p) \quad (1)$$

where f_0 is the pre-exponential factor, E_a is the activation energy, k_B is the Boltzmann constant, T_p is the peak temperature. Figure 8c,d shows the Arrhenius plot of $\ln f$ as a function of $1000/T_p$. The Arrhenius relation are quite good straight lines, the straight line fitting to Equation (1) gives the activation energy for relaxation $E_a = 1.16$ eV in the Ta-LTO and 1.07 eV in the LTO. Obviously LTO has a much wider frequency span than Ta-LTO in Figure 7a,b. It results in a relatively slight enhancement in activation energy values for Ta-doped LTO. As this may be Ta^{5+} ion to Ti^{4+} site and enhance the energy gap, the original bound electron hole is a more difficult to excite carrier, causing increased activation.

Now we turn our attention to the origin of dielectric anomaly in the Ta-LTO crystal at a temperature of around 250–300 °C in Figure 7b. As can be seen from inset of Figure 7b, the dielectric anomaly appears in the temperature where $\tan\delta$ nearly exponentially increases with temperature. This fact indeed indicates that the conductivity becomes remarkable in this temperature range that causes pronounced background. So from Figure 8a we can clearly see that a set of $M''(T)$ peaks

appear in the temperature range where the dielectric anomaly occurs. The peak shifts to higher temperature with increasing frequency indicative of a thermally activated relaxation process. So the dielectric anomaly behavior in the Ta-LTO crystal sample might be related to the oxygen vacancies. An oxygen-related dielectric anomaly has been reported in different material systems [32–34]. Two oxygen-vacancy-related relaxation processes have been reported [35]: a dipolar relaxation related to the hopping motions of oxygen vacancy and a Maxwell-Wagner relaxation as the defects were blocked by the interface on sample contacts. Typically, the dielectric relaxation of Mn-doped YFeO₃ ceramics at high temperature was originated from the polaron hopping based on the electron defect [36]. Meanwhile the dielectric relaxation of bismuth-doped La₂Ti₂O₇ ceramics in the temperature range of 600–1000 °C originates from the Maxwell-Wagner effect [37]. It is well known that oxygen vacancies can make contributions to polarization in the form of doubly charged state at high temperature ranges. For example, the activation energy for the relaxation associated with doubly ionized oxygen vacancies in NiTiO₃ was found to be 1.17 eV [38]. The activation energy value for Ta-LTO crystal samples is 1.16 eV, so the dielectric relaxation in the Ta-LTO crystal stems from the doubly charge oxygen vacancies. If the dielectric relaxation was related to the electron migration of oxygen vacancies, the polarization and conduction processes should show close values of activation energy [39]. The carrier conduction process can be understood through AC conductivity measurements.

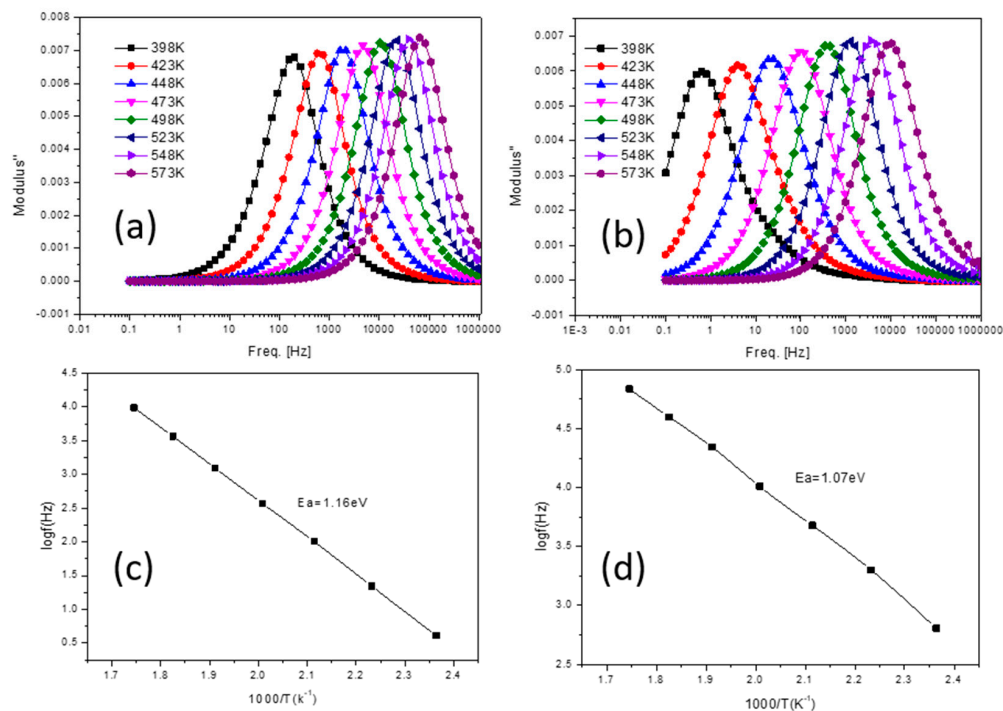


Figure 8. (a,b) are frequency dependence of the imaginary part of the electric modulus in the temperature range from 398 k to 573 k for Ta-LTO and LTO single crystals, respectively; and (c,d) are the corresponding Arrhenius plots of Ta-LTO and LTO crystals, respectively.

Figure 9 shows the variation of AC conductivity with frequency at several temperatures. The conductivity was observed to be nearly the frequency independent in the low frequency, and then exponentially increases with frequency. As seen in Figure 9, the AC conductivity is nearly constant at low frequencies and is approximately equal to DC conductivity (σ_{dc}). The plateau region extends to higher frequencies with the decrease of temperature, the σ_{dc} can be read directly and is plotted as a function of the reciprocal of temperature as shown in the insert of Figure 9. It follows the Arrhenius law:

$$\sigma_{dc} = \sigma_0 \exp\left[-\frac{E_{cond}}{k_B T}\right] \quad (2)$$

where σ_0 is the pre-exponential factor, and E_{cond} is the activation energy for conduction. The activation energy was deduced to be $E_{cond} = 0.96$ eV. It was a little smaller than the activation energy for dielectric relaxation ($E_a = 1.16$ eV), which suggests that the dielectric anomaly at temperature of about 275 °C is truly related to the hopping motions of doubly charged oxygen vacancies.

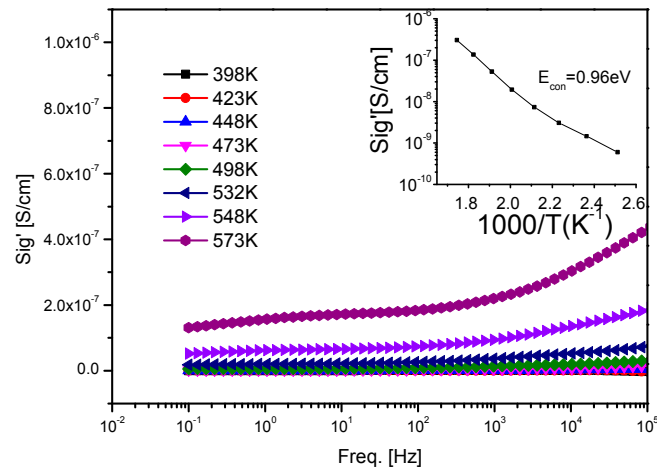


Figure 9. AC conductivity as a function of frequency at selected temperatures for Ta-LTO crystal. The inset shows the data in Arrhenius representation.

4. Conclusions

In this work, a Ta-doped La₂Ti₂O₇ single crystal of about 40 mm in length and 5 mm in diameter was successfully grown by the floating zone method in an argon atmosphere. The crystal has a monoclinic structure (P2₁) with good composition homogeneity. The dielectric properties of Ta-LTO crystal has been systematically investigated in the frequency of 10² Hz to 10⁵ Hz and a temperature range of 0–300 °C. An obvious dielectric relaxation with the activation energy of 1.16 eV was observed in the spectra of the electric modulus, which may be associated with the migration of oxygen vacancies.

Acknowledgments: The work is supported by the Nature Science Foundation of China (51572175) and the International Cooperation Program of Chinese Academy of Sciences (Y35YQ1110G).

Author Contributions: Jianding Yu conceived and designed the experiments; Huan He and Chaoyue Wang grew the single crystals; Hui Wang measured the dielectric properties; Hui Wang and Qin Li analyzed the data; Hui Wang wrote the manuscript; Jiayue Xu made the final modification. All authors read and approved the final version of the manuscript to be submitted.

Conflicts of Interest: The authors declare no conflict of interest.

References

1. Turner, R.; Fuierer, P.; Newnham, R.; Shrout, T. Materials for high-temperature acoustic and vibration sensors: A review. *Appl. Acoust.* **1994**, *41*, 299–324. [[CrossRef](#)]
2. Damjanovic, D. Materials for high temperature piezoelectric transducers. *Solid State Mater. Sci.* **1998**, *3*, 469–473. [[CrossRef](#)]
3. Zhang, S.J.; Xia, R.; Lebrun, L.; Anderson, D.; Shrout, T.R. Piezoelectric materials for high power, high temperature applications. *Mater. Lett.* **2005**, *59*, 3471–3475. [[CrossRef](#)]
4. Zhang, S.J.; Yu, F.P. Piezoelectric materials for high temperature sensors. *J. Am. Ceram. Soc.* **2011**, *94*, 17–34. [[CrossRef](#)]
5. Zhang, S.J.; Frantz, E.; Xia, R.; Everson, W.; Randi, J.; Snyder, D.; Shrout, T. Gadolinium calcium oxyborate piezoelectric single crystals for ultra-high temperature (>1000 °C) applications. *J. Appl. Phys.* **2008**, *104*, 084103. [[CrossRef](#)]

6. Zhang, S.J.; Fei, Y.; Frantz, E.; Snyder, D.; Chai, H.; Shrout, T. High-temperature piezoelectric single crystal $\text{ReCa}_4\text{O}(\text{BO}_3)_3$ for sensor applications. *IEEE Trans. Ultrason. Ferroelectr. Freq. Control* **2008**, *55*, 2703–2708. [[CrossRef](#)] [[PubMed](#)]
7. Costa, S.; Li, M.; Frade, J.; Sinclair, D.C. Modulus spectroscopy of $\text{CaCu}_3\text{Ti}_4\text{O}_{12}$ ceramics: Clues to the internal barrier layer capacitance mechanism. *RSC Adv.* **2013**, *3*, 7030–7036. [[CrossRef](#)]
8. Yamamoto, J.K.; Bhalla, A.S. Piezoelectric properties of layered perovskite $\text{A}_2\text{Ti}_2\text{O}_7$ (A = La and Nd) single-crystal fibers. *J. Appl. Phys.* **1991**, *70*, 4469. [[CrossRef](#)]
9. Nanamatsu, S.; Kimura, M.; Doi, K.; Matsushita, S.; Yamada, N. A new ferroelectric: $\text{La}_2\text{Ti}_2\text{O}_7$. *Ferroelectrics* **1974**, *8*, 511–513. [[CrossRef](#)]
10. Lichtenberg, F.; Herrnberger, A.; Wiedenmann, K. Synthesis, structural, magnetic and transport properties of layered perovskite-related titanates, niobates and tantalates of the type $\text{A}_n\text{B}_n\text{O}_{3n+2}$, $\text{A}'\text{A}_{k-1}\text{B}_k\text{O}_{3k+1}$ and $\text{A}_m\text{B}_{m-1}\text{O}_{3m}$. *Prog. Solid State Chem.* **2008**, *36*, 253–387. [[CrossRef](#)]
11. Lichtenberg, F.; Herrnberger, A.; Wiedenmann, K.; Mannhart, J. Synthesis of perovskite-related layered $\text{A}_n\text{B}_n\text{O}_{3n+2} = \text{ABO}_x$ type niobates and titanates and study of their structural, electric and magnetic properties. *Prog. Solid State Chem.* **2001**, *29*, 1–70. [[CrossRef](#)]
12. Kimura, M.; Nanmatsu, S.; Doi, K.; Matsushita, S.; Takahashi, M. Electrooptic and piezoelectric properties of $\text{La}_2\text{Ti}_2\text{O}_7$ single crystal. *Jpn. J. Appl. Phys.* **1972**, *11*, 904. [[CrossRef](#)]
13. Takahashi, J.; Kageyamal, K.; Kodaira, K. Microwave dielectric properties of lanthanide titanate ceramics. *Jpn. J. Appl. Phys.* **1993**, *32*, 4327–4331. [[CrossRef](#)]
14. Paul, A.F.; Robert, E.N. $\text{La}_2\text{Ti}_2\text{O}_7$ ceramics. *J. Am. Ceram. Soc.* **1991**, *74*, 2876–2881.
15. Yan, H.X.; Ning, H.P.; Kan, Y.; Wang, P.; Reece, M.J. Piezoelectric ceramics with super-high curie points. *J. Am. Ceram. Soc.* **2009**, *92*, 2270–2275. [[CrossRef](#)]
16. Atuchin, V.V.; Gavrilova, T.A.; Grivel, J.C.; Kesler, V.G. Electronic structure of layered ferroelectric high-k titanate $\text{La}_2\text{Ti}_2\text{O}_7$. *J. Phys. D* **2009**, *42*, 035305. [[CrossRef](#)]
17. Fasquelle, D.; Carru, J.C.; Le Gendre, L.; Le Paven, C.; Pinel, J.; Chevire, F.; Tessier, F.; Marchand, R. Lanthanum titanate ceramics: Electrical characterizations in large temperature and frequency ranges. *J. Eur. Ceram. Soc.* **2005**, *25*, 2085–2088. [[CrossRef](#)]
18. Gao, Z.; Wu, L.; Lu, C.; Wei, G.; Zhang, T.; Liu, G.; Xie, Q.; Li, M. The anisotropic conductivity of ferroelectric $\text{La}_2\text{Ti}_2\text{O}_7$ ceramics. *J. Eur. Ceram. Soc.* **2017**, *37*, 137–143. [[CrossRef](#)]
19. Orum, A.; Takatori, K.; Hori, S.; Ikeda, T.; Yoshimura, M.; Tani, T. Atomic force microscopy surface analysis of layered perovskite $\text{La}_2\text{Ti}_2\text{O}_7$ particles grown by molten flux method. *Jpn. J. Appl. Phys.* **2016**, *55*, 08NB08. [[CrossRef](#)]
20. Kim, H.G.; Hwang, D.W.; Bae, S.W.; Jung, J.H.; Lee, J.S. Photocatalytic water splitting over $\text{La}_2\text{Ti}_2\text{O}_7$ synthesized by the polymerizable complex method. *Catal. Lett.* **2003**, *91*, 193–198. [[CrossRef](#)]
21. Hwang, D.W.; Kim, H.G.; Kim, J.; Cha, K.Y.; Kim, Y.G.; Lee, J.S. Photocatalytic water splitting over highly donor-doped (110) layered perovskites. *J. Catal.* **2000**, *193*, 40–48. [[CrossRef](#)]
22. Hwang, D.W.; Cha, K.; Kim, Y.J.; Kim, H.G.; Bae, S.W.; Lee, J.S. Photocatalytic degradation of CH_3Cl over a nickel-loaded layered perovskite. *Ind. Eng. Chem. Res.* **2003**, *42*, 1184–1189. [[CrossRef](#)]
23. Cai, X.; Zhang, J.; Mamoru, F.; Tetsuro, M. Graphitic- C_3N_4 hybridized N-doped $\text{La}_2\text{Ti}_2\text{O}_7$ two-dimensional layered composites as efficient visible-light-driven photocatalyst. *Appl. Catal. B* **2017**, *202*, 191–198. [[CrossRef](#)]
24. Li, C.C.; Khaliq, J.; Ning, H.P.; Wei, X.Y.; Yan, H.Y.; Reece, M.J. Study on properties of tantalum-doped $\text{La}_2\text{Ti}_2\text{O}_7$ ferroelectric ceramics. *J. Adv. Dielectr.* **2015**, *5*, 1550005. [[CrossRef](#)]
25. Gerson, R. Variation in ferroelectric characteristics of lead zirconate titanate ceramics due to minor chemical modifications. *J. Appl. Phys.* **1960**, *31*, 188. [[CrossRef](#)]
26. Oh, Y.W.; Kim, H.; Baek, K.H.; Do, L.M.; Lee, G.W.; Kang, C.M. Effect of post-annealing on low-temperature solution-processed high-performance indium oxide thin film transistors. *Sci. Adv. Mater.* **2018**, *10*, 518–521. [[CrossRef](#)]
27. Shannon, R.D. Revised effective ionon radii and systematic studies of interatomic distances in halides and chalcogenides. *Acta Crystallogr.* **1976**, *32*, 751–767. [[CrossRef](#)]
28. Trukhanov, S.V.; Trukhanov, A.V.; Turchenko, V.A.; Trukhanov, A.V.; Trukhanova, E.L.; Tishkevich, D.I.; Ivanov, V.M.; Zubar, T.I.; Salem, M.; Kostishyn, V.G.; et al. Polarization origin and iron positions in indium doped barium hexaferrites. *Ceram. Int.* **2018**, *44*, 290–300. [[CrossRef](#)]

29. Fiedziuszko, S.J.; Holme, S. Dielectric resonators raise your high-Q. *IEEE Microw. Mag.* **2001**, *2*, 50–60. [[CrossRef](#)]
30. Wang, C.C.; Wang, J.; Sun, X.H.; Liu, L.N.; Zheng, J.; Cheng, C. Oxygen-vacancy-relaxed dielectric relaxation in $\text{Na}_{0.5}\text{K}_{0.5}\text{NbO}_3$. *Solid State Commun.* **2014**, *179*, 29–33. [[CrossRef](#)]
31. Wang, C.C.; Cui, Y.M.; Zhang, L.W. Dielectric properties of TbMnO_3 ceramics. *Appl. Phys. Lett.* **2007**, *90*. [[CrossRef](#)]
32. Wang, C.C.; Zhang, L.W. Oxygen-vacancy-related dielectric anomaly in $\text{CaCu}_3\text{Ti}_4\text{O}_{12}$: Post-sintering annealing studies. *Phys. Rev. B* **2006**, *74*. [[CrossRef](#)]
33. Wang, C.C.; Zhang, M.N.; Xia, W. High-temperature dielectric relaxation in $\text{Pb}(\text{Mg}_{1/3}\text{Nb}_{2/3})\text{O}_3$ - PbTiO_3 single crystals. *J. Am. Ceram. Soc.* **2013**, *96*, 1521–1525. [[CrossRef](#)]
34. Liu, L.N.; Wang, C.C.; Lei, C.M.; Li, T.; Wang, G.J.; Sun, X.H.; Wang, G.J.; Huang, S.G.; Li, Y.D.; Wang, H. Relaxor- and phase-transition-like behaviors in ZnO single crystals at high temperatures. *Appl. Phys. Lett.* **2013**, *102*. [[CrossRef](#)]
35. Ye, J.L.; Wang, C.C.; Ni, W.; Sun, X.H. Dielectric properties of ErFeO_3 ceramics over a broad temperature range. *J. Alloy. Compd.* **2014**, *617*, 850–854. [[CrossRef](#)]
36. Zhang, C.; Wang, X.; Wang, Z.; Yan, H.; Li, H.; Li, L. Dielectric relaxation, electric modulus and ac conductivity of Mn-doped YFeO_3 . *Ceram. Int.* **2016**, *42*, 19461–19465. [[CrossRef](#)]
37. Zhang, N.; Li, Q.J.; Huang, S.G.; Yu, Y.; Zheng, J.; Cheng, C.; Wang, C.C. Dielectric relaxations in multiferroic $\text{La}_2\text{Ti}_2\text{O}_7$ ceramics. *J. Alloy. Compd.* **2015**, *652*, 1–8. [[CrossRef](#)]
38. Li, T.; Wang, C.C.; Lei, C.M.; Sun, X.H.; Wang, G.J.; Liu, L.N. Conductivity relaxation in NiTiO_3 at high temperatures. *Curr. Appl. Phys.* **2013**, *13*, 1728–1731. [[CrossRef](#)]
39. Deng, G.C.; Li, G.R.; Ding, A.L.; Yin, Q.R. Evidence for oxygen vacancy inducing spontaneous normal-relaxor transition in complex perovskite ferroelectrics. *Appl. Phys. Lett.* **2005**, *87*. [[CrossRef](#)]



© 2018 by the authors. Licensee MDPI, Basel, Switzerland. This article is an open access article distributed under the terms and conditions of the Creative Commons Attribution (CC BY) license (<http://creativecommons.org/licenses/by/4.0/>).